

Online decoupling of the time-varying longitudinal feedback loops for improved performance in Advanced Virgo Plus

Van Dael, Mathyn; Witvoet, Gert; Swinkels, Bas; Pinto, Manuel; Bersanetti, Diego; Casanueva, Julia; Ruggi, Paolo; Mantovani, Maddalena; Spinicelli, Piernicola; de Rossi, Camilla

DOI

[10.1088/1361-6382/ad7cb9](https://doi.org/10.1088/1361-6382/ad7cb9)

Publication date

2024

Document Version

Final published version

Published in

Classical and Quantum Gravity

Citation (APA)

Van Dael, M., Witvoet, G., Swinkels, B., Pinto, M., Bersanetti, D., Casanueva, J., Ruggi, P., Mantovani, M., Spinicelli, P., de Rossi, C., Boldrini, M., & Oomen, T. A. E. (2024). Online decoupling of the time-varying longitudinal feedback loops for improved performance in Advanced Virgo Plus. *Classical and Quantum Gravity*, 41(21), Article 215008. <https://doi.org/10.1088/1361-6382/ad7cb9>

Important note

To cite this publication, please use the final published version (if applicable).
Please check the document version above.

Copyright

Other than for strictly personal use, it is not permitted to download, forward or distribute the text or part of it, without the consent of the author(s) and/or copyright holder(s), unless the work is under an open content license such as Creative Commons.

Takedown policy

Please contact us and provide details if you believe this document breaches copyrights.
We will remove access to the work immediately and investigate your claim.

PAPER • OPEN ACCESS

Online decoupling of the time-varying longitudinal feedback loops for improved performance in Advanced Virgo Plus^{*}

To cite this article: Mathyn van Dael *et al* 2024 *Class. Quantum Grav.* **41** 215008

View the [article online](#) for updates and enhancements.

You may also like

- [Large mirror surface control by corrective coating](#)
Romain Bonnand, Jerome Degallaix, Raffaele Flaminio et al.
- [The Advanced Virgo photon calibrators](#)
D Estevez, P Lagabbe, A Masserot et al.
- [Optimized radius of curvature tuning for the virgo core optics](#)
I Nardecchia, Y Minenkov, M Lorenzini et al.

Online decoupling of the time-varying longitudinal feedback loops for improved performance in Advanced Virgo Plus*

Mathyn van Dael^{1,3,**} , Gert Witvoet^{1,2}, Bas Swinkels³ ,
Manuel Pinto⁴, Diego Bersanetti⁵ , Julia Casanueva⁴ ,
Paolo Ruggi⁴, Maddalena Mantovani⁴ ,
Piernicola Spinicelli⁴ , Camilla de Rossi⁴ ,
Mattia Boldrini⁶ and Tom Oomen^{1,7} 

¹ Eindhoven University of Technology, Department of Mechanical Engineering, Control Systems Technology, Eindhoven, The Netherlands

² TNO, Optomechatronics Department, Delft, The Netherlands

³ Nikhef, Amsterdam, The Netherlands

⁴ European Gravitational Observatory (EGO), I-56021 Cascina, Pisa, Italy

⁵ INFN, Sezione di Genova, I-16146 Genova, Italy

⁶ INFN, Sezione di Roma, Piazzale Aldo Moro 2, I-00185 Roma, Italy

⁷ Delft Center for Systems and Control, Delft University of Technology, Delft, The Netherlands

E-mail: m.r.v.dael@tue.nl

Received 4 June 2024; revised 20 August 2024

Accepted for publication 18 September 2024

Published 8 October 2024



CrossMark

Abstract

Gravitational Wave detectors require low-noise sensors combined with high-performance feedback loops to maximize the detector sensitivity in the low-frequency detection range. Some feedback loops in the detector are strongly coupled and their coupling varies over time, which is inherent to the optical configuration and the optical readout scheme used to obtain error signals for the feedback loops. This paper presents a control-based approach to deal with

* This work has been funded by the Netherlands Organisation for Scientific Research (NWO) under Grant number 680.92.18.02.

** Author to whom any correspondence should be addressed.



Original Content from this work may be used under the terms of the [Creative Commons Attribution 4.0 licence](https://creativecommons.org/licenses/by/4.0/). Any further distribution of this work must maintain attribution to the author(s) and the title of the work, journal citation and DOI.

the time-varying interaction among three of the longitudinal degrees of freedom in the Advanced Virgo Plus detector, using the pre-existing infrastructure of the detector. An intuitive Multiple-Input Multiple-Output stability criterion is presented that illustrates how the time-varying coupling affects the stability of the feedback loops, as well as a method that identifies the coupling online and updates a decoupling matrix accordingly. Experiment results of the proposed method on the Advanced Virgo Plus detector illustrate continuous minimization of the coupling over time. Using the derived stability criterion, it is furthermore shown that the coupling is sufficiently minimized such that the interaction terms can be neglected in the control design, resulting in an improved controller performance.

Keywords: gravitational waves, Advanced Virgo Plus, factorized Nyquist, MIMO, decoupling, interaction

1. Introduction

Low-noise error signals for controlling the mirror positions of Gravitational Wave (GW) detectors such as Advanced Virgo Plus (AdV+) (Acernese *et al* 2023) and Advanced LIGO (Aasi *et al* 2015) are crucial for attaining the highest possible sensitivity in the low-frequency detection range. A secondary requirement for these error signals is that they are ideally well decoupled, that is, an error signal predominantly measures a single Degree of Freedom (DoF) (Bersanetti *et al* 2022), since this avoids limitations on the performance of the feedback loops and consequently the sensitivity of the detector (van Dael *et al* 2022). To obtain these error signals, the laser light sent into the interferometer is phase-modulated and subsequently demodulated in the signals of the photodiodes at the various outputs of the detector (Black 2001, Bersanetti *et al* 2022). Thus, obtaining the most suitable error signals consists of determining the optimal combination of modulation frequency and photodiode that results in sufficiently decoupled error signals with a desired noise floor (Bersanetti *et al* 2022, Valentini 2023). This is typically done using simulations of the detector, which, in practice, often still leads to considerable cross-coupling among the feedback loops.

These procedures are based only on simulations and are iteratively performed until satisfactory error signals are obtained (Bersanetti *et al* 2022, Valentini 2023). However, there are loops where sufficiently decoupled error signals are difficult to obtain due to mismatches between the simulations and the real interferometer. Using the simulation process to find more optimal error signals therefore quickly becomes a cumbersome process in terms of time and effort. Beyond the standard simulation approach to deal with strongly coupled error signals, an approach has been proposed in van Dael *et al* (2022) that deals with the problem of stability due to coupling among the loops over time and how this affects the control design, given that the coupling also varies over time. While it provides an effective design guide for the controllers, the proposed approach poses limitations on the performance of the feedback loops and thus the sensitivity of the detector.

Although important developments have been made regarding feedback loops that exhibit strong and time-varying coupling, a time-efficient control-based solution that does not pose limitations on the performance of the feedback loops is presently not available. The aim of this paper is to develop a control-based approach that exploits both model knowledge and

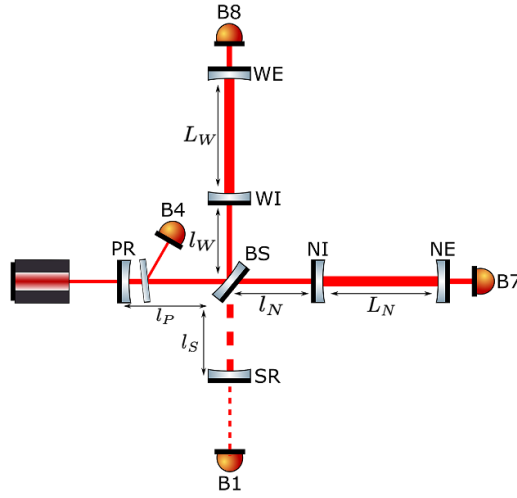


Figure 1. Part of the optical configuration of Advanced Virgo Plus for the O4 science run. The B1 photodiode measures the interference pattern between the two arms ($l_W + L_W$ and $l_N + L_N$), which change in length with opposite signs when a Gravitational Wave passes.

experimental data to solve the limitations imposed by the time-varying couplings using the pre-existing infrastructure of the detector.

The contribution of this paper is three-fold. First, a data-based approach that intuitively illustrates how the time-varying interaction affects Multiple-Input Multiple-Output (MIMO) stability of the system is derived. Second, pre-existing perturbations in the detector are used in an algorithm to identify the coupling between the DoFs. Third, an algorithm is developed that uses the identified coupling matrix to implement a decoupling matrix that combines the sensor outputs to create new decoupled error signals, where the decoupling matrix is iteratively updated to maintain a small coupling level over time without introducing large transients in the system when updating the matrix.

In section 2, the control problem addressed in this paper is formulated after which the methodology used to tackle the problem is presented in section 3. Experimental results using the proposed method from the AdV+ detector are then presented in section 4 after which section 5 provides conclusions on this work.

2. Problem formulation

2.1. System description

The optical configuration of the AdV+ detector for the current science run is depicted in figure 1. The two 3 km long orthogonal arms L_W , L_N fluctuate in length in opposing directions when a GW passes and therefore change the interference pattern, which is subsequently measured on the B1 photodiode. The optical cavities constituting the detector have to be actively controlled through feedback loops to keep the cavities on resonance and to be sensitive enough to detect the fluctuations induced by a passing GW. A total of five so-called longitudinal Degrees of Freedom (DoFs) are actively controlled, which are defined as

$$\begin{aligned}
L_{\text{DARM}} &= L_N - L_W, \\
L_{\text{CARM}} &= \frac{L_N + L_W}{2}, \\
L_{\text{MICH}} &= l_N - l_W, \\
L_{\text{PRCL}} &= l_P + \frac{l_N + l_W}{2}, \\
L_{\text{SRCL}} &= l_S + \frac{l_N + l_W}{2},
\end{aligned} \tag{1}$$

with DARM, which stands for Differential Arm, being the most important DoF as it contains the GW signal. Each DoF except for CARM is controlled using a feedback loop that uses the powers on the photodiodes in combination with the Pound–Drever–Hall method (Black 2001), or a DC signal in the case of DARM, to obtain an error signal. The correction signal based on these error signals is then applied to the actuators on a combination of mirrors to actively control the length of the DoFs and reject disturbances. The CARM loop uses a more elaborate control structure (van Dael *et al* 2025) and is not considered in this paper.

2.2. Time-varying coupling

The focus of this paper is on a problem concerning 3 of the 5 longitudinal DoFs, commonly referred to as the Central Interferometer (CITF) DoFs, which are MICH, PRCL and SRCL. These auxiliary DoFs to the DARM DoF are known to be strongly coupled due to a combination of the optical configuration and the used sensing mechanism, i.e. the sensors detect a combined motion of the DoFs and the system input-output relation is thus strongly coupled among the DoFs.

The MIMO frequency response of the CITF DoFs can be described by

$$H(j\omega) = G_i A(j\omega), \tag{2}$$

with $H(j\omega) \in \mathbb{C}^{3 \times 3}$ representing the frequency response of the plant from actuation on the mirrors to the powers on the photodiode. The plant is split into two parts, the mechanical response of the mirrors $A(j\omega) \in \mathbb{C}^{3 \times 3}$ relating the voltage sent to the actuators to a change in length of the DoFs, and the optical plant $G_i \in \mathbb{R}^{3 \times 3}$ relating a change in length of the DoFs to the Pound–Drever–Hall error signal. The subscript i in G refers to a realization of the time-varying matrix $G(t)$, which is assumed to be valid in a time window between t_i and t_{i+1} ,

$$G(t) \approx G_i \forall t \in [t_i \ t_{i+1}]. \tag{3}$$

The time dependency in G stems from thermal transients and changes in the optical alignment, changing the optical response of the interferometer. Note here that the timescale of the changes in G_i is orders of magnitude slower than the plant dynamics of $H(j\omega)$. In figure 2, the Frequency Response Matrix (FRM) of $H(j\omega)$ is shown, where $H(j\omega)$ is measured at three different time instances. While the diagonal terms, on which the controllers are designed, remain the same, the off-diagonal terms vary in magnitude over time.

In figure 3, a stability criterion is presented based on the FRMs from figure 2, of which the full criterion and its interpretation are derived in section 3.1. The dashed colored lines represent a stability bound based on the off-diagonal terms of figure 2 and the black line represents the SISO closed-loop transfer function for one of the loops, which has to remain below the stability bound to guarantee MIMO stability. This SISO loop violates the criterion for two of the three measured coupling instances, meaning MIMO stability cannot be guaranteed at all times.

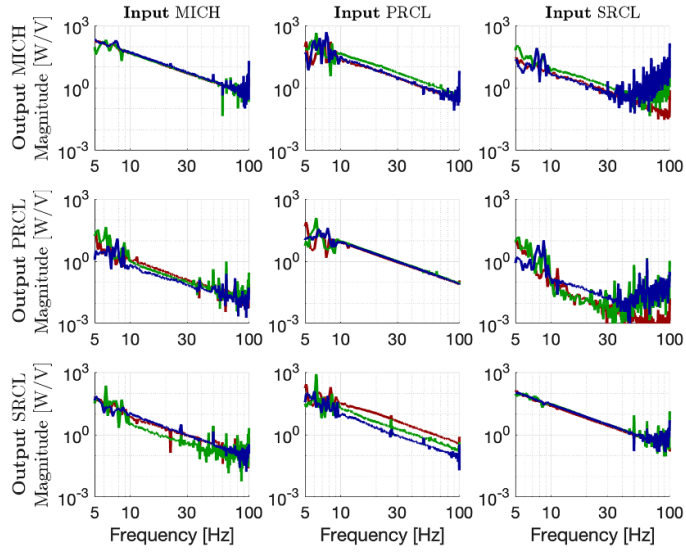


Figure 2. Magnitude of three different Frequency Response Matrix measurements of H , represented by (—), (—) and (—), measured at least two weeks apart. The diagonal terms remain the same, while the off-diagonal terms vary in magnitude over time due to thermal transients and changes in the relative alignment between the mirrors.

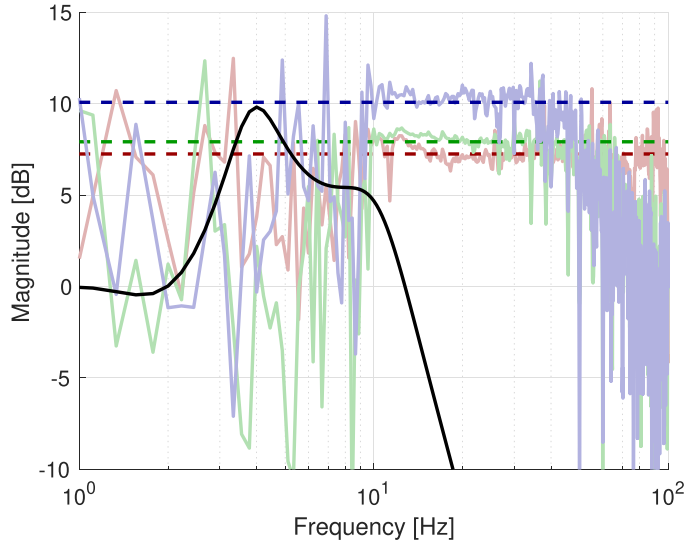


Figure 3. Stability and robustness assessment using the Factorized Nyquist criterion, with $\tilde{T}_M(j\omega)$ (—) plotted against $\mu_{\tilde{T}}^{-1}(E(j\omega))$, which are computed based on the FRFs presented in figure 2 and represented by (—), (—) and (—). Estimates of α are represented by (—), (—) and (—), by computing mean value of $\mu_{\tilde{T}}^{-1}(E(j\omega))$ at frequency bins with coherence higher than 0.8. It is shown that the condition of (17) is violated for the present level of coupling and control design. The derivation and complete interpretation of this figure are delineated in section 3.1.1.

There are two possible solutions to the problem of large coupling. The first is to adjust the controller design such that MIMO stability is guaranteed in the presence of all possible interactions, i.e. reduce the peak of the black line in figure 3 such that it remains below the stability bound for each time instance. The downside of the proposed method is however that the control design requires large stability margins to reduce the peak, which goes at the expense of the roll-off of the controller at high frequencies and therefore may introduce more noise in the DARM loop due to the coupling between the CITF DoFs and DARM. The second solution, which is pursued here, is to increase the stability bound such that there are no design restrictions on the SISO loops anymore.

2.3. Reducing interaction through decoupling

To increase the stability bounds in figure 3, static decoupling (Lee *et al* 2005) is applied. Static decoupling is typically the first tool in MIMO control designs to decouple the system and obtain SISO loops. There are several methods to derive the decoupling matrices. A basic approach is to use matrix decomposition methods (MacFarlane 1970, Owens 1978, Hung and MacFarlane 1982), which decouples the system in a specific frequency range if the MIMO system is not symmetric. Alternative approaches that aim to minimize the coupling across the entire frequency band have also been proposed (Vaes *et al* 2004, Stoev *et al* 2017). The approach taken in this paper is however much more straightforward as the specific structure of the system is exploited to derive the decoupling matrix. Since the coupling is predominantly present in G_i , the interaction is minimized by applying a decoupling matrix T_y that is the inverse of G_i , i.e.

$$T_y^{\text{opt}} = G_i^{-1}. \quad (4)$$

This decoupling matrix is optimal, hence the superscript *opt*, since the decoupled system would then approximate $A(j\omega)$ in the time window $[t_i \ t_{i+1}]$, which is assumed to be diagonal due to the assumed perfect decoupling of the actuation. The decoupled system would then be free of any MIMO design restrictions on the controllers and thus can have arbitrarily small stability margins to maximize the roll-off at high frequencies. This requires batch-wise updating of the decoupling matrix T_y since G varies over time. Note furthermore that an output transformation is used, which is a conscious choice since the plant coupling stems from the sensors. The proposed method is however also possible to implement using an input transformation using the same mathematical derivations as presented in this paper.

2.4. Experimental conditions

The proposed method requires batch-wise identification of G_i . The frequency response identification of G_i is fairly straightforward when there are no restrictions on the perturbation signals, but it is undesired to continuously inject perturbation signals such as white noise or multisines as this spoils the detector sensitivity. Only a single sinusoid per DoF is therefore used for the identification procedure. This perturbation is permanently on as it is also used for monitoring and calibration purposes and is thus readily available.

2.5. Problem formulation

The general problem addressed in this paper is how to deal with the time-varying interaction in the system. To this end, a tool is first required that illustrates how the time-varying aspect affects the MIMO stability criterion. This tool is furthermore required to address the

effectiveness of the decoupling procedure and determine whether sufficient decoupling is attained to render the interaction negligible. The second subproblem is how to perform the identification given the available perturbation signal since the typical identification approach for line perturbations does not suffice, as is shown in section 3.2.

3. Methodology

The first part of this section derives the MIMO design criterion used to identify how the time dependency of the plant affects MIMO stability and how this criterion can be applied to the particular control problem addressed in this paper. Second, an identification procedure is derived which uses the readily available perturbation signals in AdV+ to identify the time-varying part of the plant G_i , which is later used to derive the decoupling matrix T_y .

3.1. MIMO stability for time-varying interaction

There are several MIMO stability analysis tools available in the literature to assess closed-loop stability, e.g. the Generalized Nyquist criterion (Desoer and Wang 1980), which provides a necessary and sufficient condition for MIMO stability. The difficulty of these tools with respect to the control problem in this paper is that it is not necessarily intuitive how to tune the controllers to obtain MIMO stability and robustness given the time-varying interaction.

The method used in this paper to assess MIMO stability in view of the time-varying interaction is the Factorized Nyquist criterion, originally presented in Grosdidier and Morari (1986). A derivation of this criterion is presented next after which the criterion is applied to the control problem in AdV+.

3.1.1. Factorized Nyquist criterion. Consider the system H as defined in (2), of which the diagonal elements are denoted by

$$\tilde{H} = \text{diag}(H) \quad (5)$$

and the coupling matrix E is given by

$$E = (H - \tilde{H}) \tilde{H}^{-1}, \quad (6)$$

such that the plant can be rewritten to

$$H = (I + E) \tilde{H}. \quad (7)$$

Using (7), the MIMO sensitivity function can be factorized into two products

$$(I + HK)^{-1} = \underbrace{(I + \tilde{H}K)^{-1}}_{\tilde{S}} \underbrace{(I + E\tilde{T})^{-1}}_{\text{Interaction}}, \quad (8)$$

with

$$\tilde{T} = \tilde{H}K(I + \tilde{H}K)^{-1} \quad (9)$$

the complementary sensitivity of the diagonal terms, K the diagonal MIMO controller and \tilde{S} the MIMO sensitivity of the diagonal plant \tilde{H} , which is thus also a diagonal system since K is diagonal. The MIMO closed-loop system is then stable if both MIMO transfer functions on the right in (8) are stable. The first term \tilde{S} is stable by design since the controller K is designed such that the SISO loops are stable. Note furthermore that the time-varying effect does not affect the diagonal elements and therefore also not \tilde{S} .

The second term is referred to as the interaction term since the coupling matrix E only contains the off-diagonal elements. The stability of the interaction term is analyzed using the small-gain theorem (Zames 1966), i.e. the interaction term is stable if

$$I + E(j\omega)\tilde{T}(j\omega) > 0 \forall \omega, \quad (10)$$

which is equivalent to

$$\bar{\sigma}(E(j\omega)\tilde{T}(j\omega)) < 1 \forall \omega, \quad (11)$$

with $\bar{\sigma}$ the maximum singular value. Rewriting (11) to

$$\bar{\sigma}(\tilde{T}(j\omega)) < \bar{\sigma}^{-1}(E(j\omega)) \forall \omega, \quad (12)$$

then yields a criterion in which the left side is dependent on the control design K , while the term on the right only depends on E which is a function of the system dynamics. The term $\bar{\sigma}^{-1}(E(j\omega))$ can thus be computed based on the measured frequency response of H and the controller K is then designed such that (12) is satisfied.

The stability condition of (12) will lead to a conservative control design, in part because of the bound $\bar{\sigma}^{-1}(E(j\omega))$. This term provides the maximum gain of E at each frequency but neglects the specific structure of $\tilde{T}(j\omega)$, which in this case is diagonal. To increase the stability bound and thus provide more freedom in the control design of K and therefore $\tilde{T}(j\omega)$, the Structured Singular Value (SSV), see Packard and Doyle (1993) for the mathematical derivation, is instead used. The SSV provides the maximum gain of E with respect to the diagonal structure of $\tilde{T}(j\omega)$, allowing to formulate the stability condition of (12) for each DoF as

$$|\tilde{T}_i(j\omega)| < \mu_{\tilde{T}}^{-1}(E(j\omega)) \forall \omega, i, \quad (13)$$

where $\mu_{\tilde{T}}(E(j\omega))$ denotes the SSV of E with respect to the structure of \tilde{T} and \tilde{T}_i are the diagonal elements of \tilde{T} . The design criterion amounts to tuning the SISO loops such that their complementary sensitivity function for all frequencies remains below the inverse of the SSV μ , which is computed from a measured frequency response.

3.1.2. Factorized Nyquist criterion for AdV+. The Factorized Nyquist criterion is applied to the CITF DoFs of AdV+. The specific plant structure of the CITF DoFs allows the simplification of the criterion. Since the Unity Gain Frequencies (UGFs) of the loops are in the 1 to 100 Hz range, stability analysis is of primary interest in this frequency range. The plant is approximated in this frequency range by

$$H(j\omega) = A(j\omega)G_i \approx \frac{1}{(j\omega)^2}G_i \quad (14)$$

since the actuation dynamics $A(j\omega)$ are approximately the same for all three loops and can be approximated by a -2 slope in the frequency range of interest. Using this structure, the term E then amounts to

$$E = \left(\frac{1}{(j\omega)^2} (G_i - \tilde{G}_i) \right) (j\omega)^2 \tilde{G}_i^{-1} = (G_i - \tilde{G}_i) \tilde{G}_i^{-1}. \quad (15)$$

The term E thus becomes frequency-independent given the specified structure of the plant in (14). It therefore also follows that the SSV μ is frequency-independent, i.e.

$$\mu_{\tilde{T}}(E(j\omega)) = \alpha \forall \omega \in 2\pi [1 \ 100]. \quad (16)$$

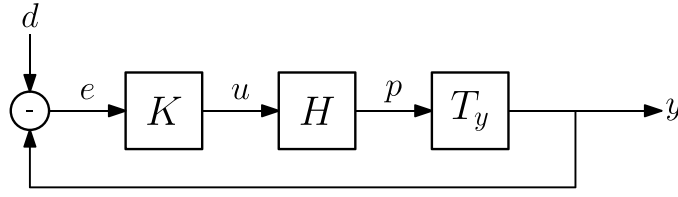


Figure 4. Block diagram of the control system used to control the longitudinal degrees of freedom in AdV+.

The design criterion in (13) then reduces to

$$\|\tilde{T}_i(j\omega)\|_\infty < \alpha^{-1}, \quad (17)$$

where the H_∞ norm is the maximum magnitude of the transfer function over all frequencies. This provides an intuitive insight since the time dependency in G changes the term α , so robustness is achieved by designing the controller such that the left-hand side of (17) is sufficiently small against variations of α .

3.1.3. Assessment of criterion using AdV+ data. In figure 3, the Factorized Nyquist criterion from (17) is depicted, plotting the μ values computed based on the FRF of figure 2 against \tilde{T}_M , which is the complementary sensitivity of the MICH loop. The peak value of \tilde{T}_M is around 4 Hz, which is roughly the UGF of the loop. The FRM matrix is not accurate at this frequency range and the μ estimates are therefore very noisy below 10 Hz. The μ values are frequency independent, thus allowing to average μ at the accurately identified frequency bins (between 10 and 30 Hz) and extrapolating this to lower frequencies such that the condition of (17) can be analyzed. This is another advantage of this method as it does not require an accurate FRM across a wide frequency range to assess stability.

The dashed lines in figure 3 represent the mean values of μ . The condition of (17) is violated around 4 Hz, indicating that the interaction between the DoFs is too high to guarantee MIMO stability. Note that (17) is only a sufficient condition, i.e. a violation of the condition as in figure 3 does not necessarily imply instability of the loops. Given the level of interaction, MIMO stability could be guaranteed by sufficiently reducing the peak value of \tilde{T}_M , which requires increasing the stability margins of the loop.

The Factorized Nyquist criterion provides a clear design guide on how to tune the controller for MIMO stability against the time dependency of the plant. The CITF DoFs are however known to strongly couple to the DARM DoF above 10 Hz, which is the start of the detection band. Higher stability margins will go at the expense of the roll-off of the control loops, thus introducing more noise into the DARM DoF, which is highly undesirable. The decoupling approach is therefore derived next since this allows to significantly increase the μ bound, which in turn removes the control design restrictions currently imposed by the large interaction terms.

3.2. Identification of coupling matrix: a local model approach

This section derives the identification scheme used to estimate the coupling matrix G_i using the presently available perturbation signals in AdV+. First, the identification setting is presented, after which the proposed method of identification is derived for a general control structure. In the final part, the derived identification method is applied to AdV+.

3.2.1. Identification setting. A general control structure as defined in the block diagram in figure 4 is considered here to illustrate the working principle of the method as well as its generality. Later on, the proposed method is applied to the specific plant dynamics considered in this paper. The plant $H(j\omega) \in \mathbb{C}^{n \times n}$ of dimension n is to be identified in closed-loop with a controller $K(j\omega) \in \mathbb{C}^{n \times n}$. The plant has the following structure

$$H(j\omega) = h(j\omega) \mathcal{H} \quad (18)$$

where $h(j\omega) \in \mathbb{C}^{n \times n}$ is a diagonal transfer matrix and $\mathcal{H} \in \mathbb{R}^{n \times n}$ a real matrix. The output transformation matrix $T_y \in \mathbb{R}^{n \times n}$ is for the moment considered to be an Identity matrix, i.e. $p = y$. A measurement of the error signal $e \in \mathbb{R}^n$ and control input $u \in \mathbb{R}^n$ is furthermore available as well as the perturbation signal $d \in \mathbb{R}^n$. The perturbation d is a single sinusoid per DoF, i.e.

$$d = \begin{bmatrix} A_1 \cos(\omega_1 t) \\ A_2 \cos(\omega_2 t) \\ \vdots \\ A_n \cos(\omega_n t) \end{bmatrix}, \quad (19)$$

with ω_i , $i = 1, 2, \dots, n$ the excitation frequencies which are all distinct. The objective is to identify \mathcal{H} using only the defined perturbation d . The frequency response of $h(j\omega)$ is furthermore assumed to be available, which could be obtained either through modeling or from measurements.

Discrete-time signals are used throughout this section, i.e. the signal $\hat{x}(lT_s)$ with length N is a measurement of the variable x and subject to noise. The Discrete Fourier Transform (DFT) of these signals is given by Pintelon and Schoukens (2012)

$$X(k) = \frac{1}{\sqrt{N}} \sum_{l=0}^{N-1} \hat{x}(lT_s) e^{-j2\pi lk/N}. \quad (20)$$

3.2.2. Identification using sine excitations. A typical approach in system identification to identify an $n \times n$ system is to perform n experiments where multisines are consecutively injected in orthogonal directions. An example of orthogonality is to inject it first in loop 1, then loop 2 and so on, but other orthogonal excitations are also possible. For each discrete frequency bin k , the following matrices are then constructed according to Pintelon and Schoukens (2012)

$$\mathbf{X}(k) = \begin{bmatrix} X_1^1(k) & X_1^2(k) & \dots & X_1^n(k) \\ X_2^1(k) & X_2^2(k) & \dots & X_2^n(k) \\ \vdots & \vdots & \ddots & \vdots \\ X_n^1(k) & X_n^2(k) & \dots & X_n^n(k) \end{bmatrix} \quad (21)$$

for $\mathbf{X} = \mathbf{U}, \mathbf{Y}$. The variable $X_n^m(k)$ denotes output n in experiment m at the excited frequency bin k . The plant H at the frequency bin k is then obtained by computing

$$H(k) = \mathbf{Y}(k) \mathbf{U}(k)^{-1}. \quad (22)$$

Note furthermore that for this approach $h(j\omega)$ does not need to be known. A similar approach is taken for the perturbation considered here, where each sinusoid is considered as

a separate experiment and all experiments are thus simultaneously performed. The following matrix is then constructed

$$\mathbf{X} = \begin{bmatrix} X_1^{k_1} & X_1^{k_2} & \dots & X_1^{k_n} \\ X_2^{k_1} & X_2^{k_2} & \dots & X_2^{k_n} \\ \vdots & \vdots & \ddots & \vdots \\ X_n^{k_1} & X_n^{k_2} & \dots & X_n^{k_n} \end{bmatrix} = [X^{k_1} \quad X^{k_2} \quad \dots \quad X^{k_n}], \quad (23)$$

Note the different notation in (23) where $X_i^{k_m}$ represents the DFT of output x_i , evaluated at frequency bin k_m . The columns thus represent the vector evaluated at the different frequencies. While a full matrix is obtained, (22) cannot directly be computed since the columns are at different frequencies due to the requirement of the sinusoids being at distinct frequencies.

3.2.3. Integrating local model knowledge. The frequency dependence of the columns in (23) is solved by integrating a locally valid model of the plant in the identified frequency range in the identification procedure. Consider the following input-output relation of the plant

$$\begin{bmatrix} Y_1^{k_m} \\ Y_2^{k_m} \\ \vdots \\ Y_n^{k_m} \end{bmatrix} = h(j\omega_{k_m}) \mathcal{H} \begin{bmatrix} U_1^{k_m} \\ U_2^{k_m} \\ \vdots \\ U_n^{k_m} \end{bmatrix} \quad (24)$$

for a frequency k_m . Left multiplication of both sides with the inverse of $h(j\omega_{k_m})$, which is assumed to be available, results in

$$h(j\omega_{k_m})^{-1} Y^{k_m} = \mathcal{H} U^{k_m}. \quad (25)$$

The only unknown is now \mathcal{H} , which is frequency independent, since $h(j\omega_{k_m})$ is assumed to be known and U^{k_m}, Y^{k_m} are measured. Evaluating (25) for the n DoFs and writing this in matrix form then yields

$$\underbrace{\begin{bmatrix} h(j\omega_{k_1})^{-1} Y^{k_1} & h(j\omega_{k_2})^{-1} Y^{k_2} & \dots & h(j\omega_{k_n})^{-1} Y^{k_n} \end{bmatrix}}_{\tilde{\mathbf{Y}}} = \mathcal{H} \underbrace{\begin{bmatrix} U^{k_1} & U^{k_2} & \dots & U^{k_n} \end{bmatrix}}_{\mathbf{U}}. \quad (26)$$

An estimate of \mathcal{H} is now obtained from

$$\mathcal{H} = \tilde{\mathbf{Y}} \mathbf{U}^{-1}. \quad (27)$$

The method essentially normalizes the DFT outputs by multiplying them by the inverse of the frequency-dependent part of the plant. A frequency-independent input-output relation is then found which is easily evaluated. The inverse of \mathbf{U} is furthermore guaranteed to exist since the perturbation is by definition orthogonal (one sinusoid per DoF) and the matrix is therefore always full rank.

It is furthermore not required that the complete frequency response of $h(j\omega)$ is known. Decoupling is typically applied in the frequency range around the UGF of the loops, so a model of $h(j\omega)$ is only required in this frequency range. As is shown in section 4.1.1, only the structure of $h(j\omega)$ is required, assuming all diagonal terms have the same structure in the applied frequency range. Any relative scaling between the diagonal terms is then estimated together with \mathcal{H} and compensated for in the decoupling matrix.

4. Experimental results

This section presents the implementation and experimental results of the proposed methods on the AdV+ detector.

4.1. Implementation of decoupling algorithm

The following subsection discusses the implementation aspects of the proposed approach for AdV+. First, the identification scheme is defined for the perturbation signals and system structure of the detector. Then, the update law of the decoupling matrix T_y is presented, which ensures that the coupling remains small during the update of the matrix without introducing large transients in the system.

4.1.1. Identification on AdV+. The objective is to decouple the CITF DoFs in the 1 to 100 Hz range since the UGF of the loops is in this range. The following perturbation signal is used for the identification in AdV+

$$d = \begin{bmatrix} d_M \\ d_P \\ d_S \end{bmatrix} = \begin{bmatrix} A_M \cos(2\pi 21.7t) \\ A_P \cos(2\pi 64.4t) \\ A_S \cos(2\pi 26.6t) \end{bmatrix}, \quad (28)$$

where the subscripts M, P, S denote respectively the MICH, PRCL and SRCL DoFs. Note that the excitation frequencies are chosen to be slightly above the UGF of the loops and are furthermore unique with respect to all DoFs in the detector.

A complete model of $A(j\omega)$ is not available, so the approximation as used in (14) is used as prior knowledge to estimate the frequency-dependent part of the plant, i.e.

$$h(j\omega) = A(j\omega) \approx \frac{1}{(j\omega^2)} I, \quad (29)$$

resulting in the approximation given in (14), where the -2 slope in the actuation stems from the force exerted on the mirrors, which above the resonance frequency of the suspension is approximated by a mass line. The input-output matrices U , \tilde{Y} as in (26) are then constructed according to

$$\underbrace{\begin{bmatrix} (j\omega_{k_M})^2 Y_M^{k_M} & (j\omega_{k_P})^2 Y_M^{k_P} & (j\omega_{k_S})^2 Y_M^{k_S} \\ (j\omega_{k_M})^2 Y_P^{k_M} & (j\omega_{k_P})^2 Y_P^{k_P} & (j\omega_{k_S})^2 Y_P^{k_S} \\ (j\omega_{k_M})^2 Y_S^{k_M} & (j\omega_{k_P})^2 Y_S^{k_P} & (j\omega_{k_S})^2 Y_S^{k_S} \end{bmatrix}}_{=\tilde{Y}} = G_i \underbrace{\begin{bmatrix} U_M^{k_M} & U_M^{k_P} & U_M^{k_S} \\ U_P^{k_M} & U_P^{k_P} & U_P^{k_S} \\ U_S^{k_M} & U_S^{k_P} & U_S^{k_S} \end{bmatrix}}_{=U}, \quad (30)$$

where e.g. $Y_M^{k_P}$ represents the DFT of the MICH output at the PRCL line. An estimate of the real coupling matrix is then found by computing (27).

4.1.2. Implementation of decoupling matrix. The aforementioned identification is performed on the decoupled plant

$$y = T_y H u, \quad (31)$$

so for each subsequent iteration after the first, the decoupled plant is estimated and a new T_y matrix is computed accordingly. The identification is performed by measuring the signals for 180 s, such that 18 averages are performed on 10 s periods of data. Note that 10 S periods or integer multiples of those are required since the least common divisor of the perturbation signals in (28) is 0.1 Hz.

To avoid large transients when updating the T_y matrix, the following update law is used

$$T_y(m) = T_y^{\text{old}} + \frac{m}{F_s t_{\text{ramp}}} (T_y^{\text{new}} - T_y^{\text{old}}), \quad (32)$$

with m denoting the sample index, t_{ramp} the time to switch between decoupling matrices and F_s the sampling frequency. Using this update law preserves the relative gains between the elements in the T_y matrix such that the coupling does not worsen during the updates of the weights. This can be shown by considering a static coupling matrix G_i , for which the coupling during the update of the T_y matrix is given by

$$T_y(m) G_i(m) = T_y^{\text{old}} G_i + \alpha(m) (T_y^{\text{new}} - T_y^{\text{old}}) G_i, \quad (33)$$

with

$$\alpha(m) = \frac{m}{F_s t_{\text{ramp}}} \in [0, 1]. \quad (34)$$

Equation (33) is rewritten to

$$T_y(m) G_i(m) = (1 - \alpha(m)) T_y^{\text{old}} G_i + \alpha(m) T_y^{\text{new}} G_i \quad (35)$$

and if the following condition holds

$$(T_y^{\text{new}} G_i)^{p,q} < (T_y^{\text{old}} G_i)^{p,q} \quad \forall p, q, \quad (36)$$

then

$$G_i^{\text{dec}^{p,q}}(m) < G_i^{\text{dec}^{p,q}}(m-1) \quad \forall m, p, q, \quad (37)$$

with

$$G_i^{\text{dec}^{p,q}}(m) = T_y(m) G_i(m), \quad (38)$$

where p, q denote respectively the row and column of the matrix and the superscript *dec* refers to the decoupled version of G_i . Switching times t_{ramp} of more than 10 s are used to minimize transients, so the proposed update law ensures that the coupling does not worsen in between updates and cause potential stability problems.

4.2. Decoupling over time

The coupling is measured over time to evaluate the time dependence of the effect using the identification method as defined in section 3.2. But rather than estimating the coupling at a single time instance as done in section 3.2, a moving average estimate of $T_y G(t)$ is obtained to assess how the coupling fluctuates over time as a validation method. This moving average is obtained by multiplying each time domain signal by the Euler coefficient for each perturbation frequency, i.e.

$$\tilde{x}^{k_m} = x(lT_s) e^{-j2\pi k/N}. \quad (39)$$

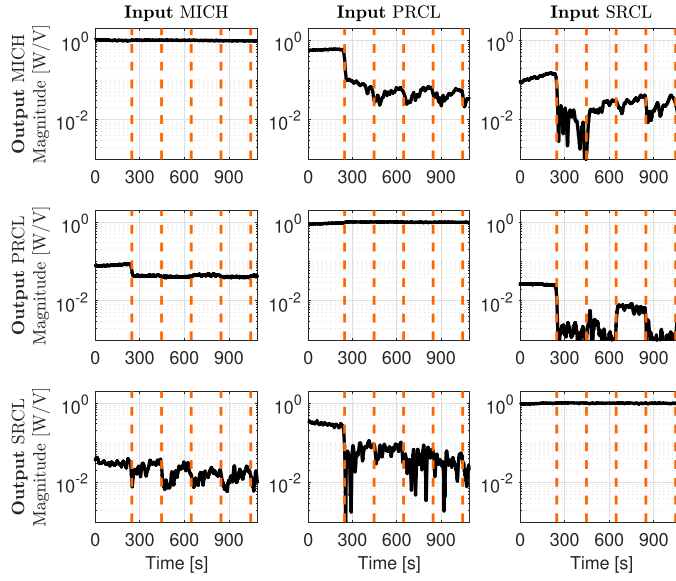


Figure 5. — Measured estimate of the decoupled coupling matrix $T_y G(t)$ over time on AdV+ and (—) are the time instances at which the output matrix T_y is updated. The coupling matrix is estimated by computing a moving average transfer function over the lines. The off-diagonal entries of $T_y G(t)$ are shown to decrease after each update and rise in amplitude in between updates of the T_y matrix.

A moving average filter is then applied to the signal \tilde{x}^{k_m} to obtain

$$X_{\text{ma}}^{k_m}(l) = \frac{1}{V} \sum_{v=0}^V \tilde{x}^{k_m}(v) q^{-v}, \quad (40)$$

where q denotes the shift operator, $x = \hat{u}, \hat{y}$ and V the number of coefficients. The variable $X_{\text{ma}}^{k_m}(l)$ thus gives a moving average of the signal \hat{x} over the DFT bin k for each discrete time instance l .

The resulting plot using this method is shown in figure 5. The vertical red dashed lines indicate the time instances at which the algorithm updates the decoupling matrix T_y . The coupling is indeed shown to reduce at these time instances, with the largest jump at the first iteration and a few smaller jumps at subsequent iterations. The effect of the thermal transient and other effects changing the coupling levels are also observed in e.g. the 1,2 element, where the coupling increases in between the time instances.

4.3. Coupling through Factorized Nyquist

Based on the moving average estimate of $G(t)$ obtained in section 4.2, $\mu_{\tilde{T}}(E)$ is computed over time and compared against the H_∞ norms of the complementary sensitivity functions of the individual loops to assess stability. The criterion over time is depicted in figure 6⁸, where the marked black lines represent the H_∞ norms of the MICH, PRCL and SRCL loops and

⁸ Note that the cyan line represents $\mu(E)$ over time, which is the same variable as plotted in figure 3, but the starting value is slightly higher since this measurement is taken at a different time instance during the thermal transient.

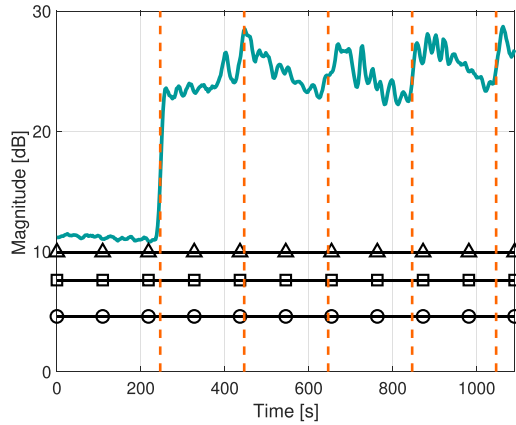


Figure 6. Factorized Nyquist criterion over time as defined in (17), with (\blacktriangle) MICH DoF $\|\tilde{T}_M(j\omega)\|_\infty$; (\ominus) PRCL DoF $\|\tilde{T}_P(j\omega)\|_\infty$; (\boxminus) SRCL DoF $\|\tilde{T}_S(j\omega)\|_\infty$; (—) SSV $\mu_{\tilde{T}}^{-1}(E)$ over time; (---) Update instances of the decoupling algorithm. After the first update instance, the μ bound is shown to be sufficiently high such that even for a factor four reduction MIMO of μ^{-1} , stability is guaranteed.

the cyan line is a moving average estimate of the SSV over time. It shows that in the first 220 s, the MICH loop is very close to violating the stability condition and stability thus cannot be guaranteed. After the first update instance around 220 s, $\mu_{\tilde{T}}^{-1}(E)$ is shown to increase by a large factor, such that there is a large stability margin against the fluctuating interaction terms. Several subsequent iterations are shown to increase the SSV again while it decreases in between the time updates. This highlights the necessity of continuously adapting the T_y matrix since a single computation of the weights does not guarantee the robustness margin to remain sufficiently large throughout the transient of the system.

4.4. Decoupling over broad frequency range

As a final validation of the method, the FRM is measured in the 1 to 100 Hz range without and with the decoupling approach applied to assess if the coupling is decreased over the entire frequency band. The interferometer is first left to converge to a more steady-state situation in which most of the thermal transient has passed, after which the injections are performed. First, the situation without decoupling is measured using band-passed filtered white noise in the 10 to 100 Hz range. Two iterations of the decoupling procedure are then performed after which the same measurement is repeated. The resulting FRM for both situations is depicted in figure 7.

The decoupling procedure is shown to significantly reduce the coupling in the measured frequency range. This indicates that the model used for the actuation defined in (14) is indeed accurate. The only outlier is the MICH to PRCL coupling, where the coupling for higher frequencies increases, while for the other elements the coupling is decreased by the same factor across the identified frequency range. This indicates a mismatch in the model in (14), which likely stems from the optical transfer function G_i having some frequency-dependent dynamics in this element. Note furthermore that in e.g. the MICH to SRCL element, the coupling is not

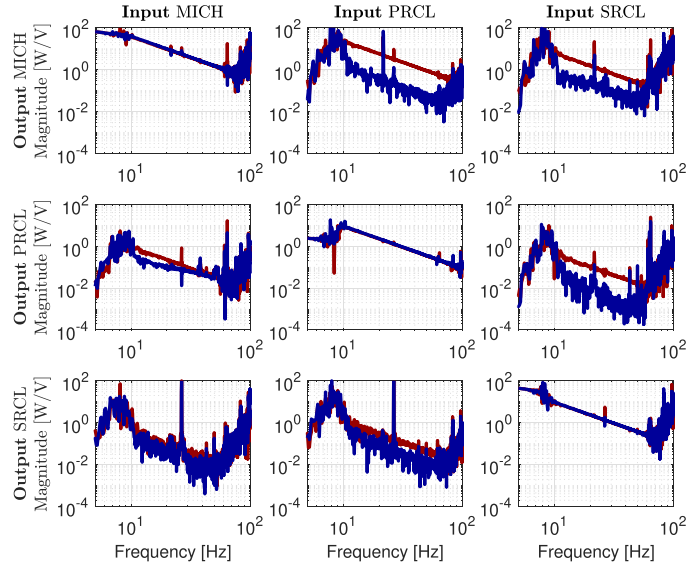


Figure 7. FRM of the plant H of the CITF DoFs on AdV+. (—) FRM when no decoupling is applied, i.e. $T_\gamma = I$, and (—) FRM when decoupling is applied. The couplings in all off-diagonal entries are decreased using the presented method, with the PRCL to MICH and SRCL to MICH couplings in particular being reduced up to a factor of 20.

reduced, which likely stems from the fact that the coupling is already very low and the coupling estimate of the element is too noisy to further reduce the coupling. The result nevertheless confirms that the approach works over the whole frequency range of interest (1 to 100 Hz) under the assumptions that are made.

4.5. Improved controller design

The objective of the proposed approach is to free the controllers from any design restrictions imposed by the coupling among the loops, i.e. the additional stability margins that are required in the SISO loops. In figure 8, the open-loop and closed-loop frequency response of the pre-existing and new MICH controller are depicted, where the new controller is the same as the one used in figure 3. Noise in the CITF loops couple to the DARM DoF through the complementary sensitivity function. Improving the roll-off of the controller in the detection band (> 10 Hz) thus reduces this noise.

The roll-off of the new controller is significantly reduced compared to the pre-existing controller, at the expense of a higher peak in the complementary sensitivity (and in general lower but still sufficient stability margins). This increased peak magnitude in the complementary sensitivity is however not a problem anymore for stability when the decoupling is applied, as illustrated in figure 6, whereas without the decoupling only the pre-existing controller would have guaranteed MIMO stability. The new controller thus reduces the noise coupling to the sensitivity of the detector, while maintaining the same level of RMS error in the loop.

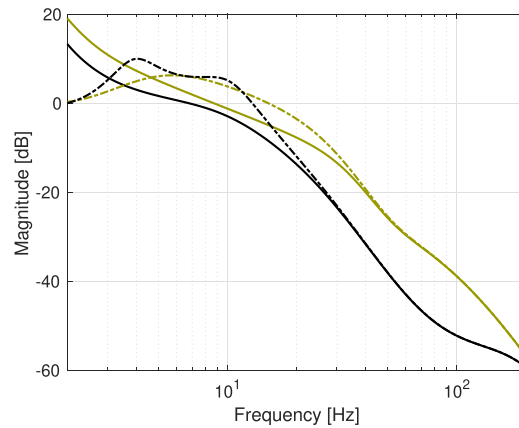


Figure 8. Magnitude of frequency response of (—) open-loop and (---) complementary sensitivity T of new MICH controller and (—) open-loop and (---) complementary sensitivity T of old MICH controller. Noise in the MICH loop couples to the sensitivity of the detector through the complementary sensitivity function, of which the roll-off is significantly lower for the new controller, thus reducing the noise coupling to the sensitivity of the detector.

5. Conclusion

A systematic design procedure has been presented in this paper that addresses the problem of controlling strongly coupled feedback loops in which the interaction varies over time, posing potential closed-loop stability problems. First, it has been shown that the Factorized Nyquist criterion is an effective tool in analyzing the time-varying behavior of the interaction terms and how this affects MIMO stability. Second, the derived identification scheme has been shown to provide a sufficiently accurate estimate of the optical plant, where the identification is continuously performed during the operation of the detector without requiring extra perturbations beyond the ones presently available in the detector. Finally, an update law for the decoupling matrix is presented that avoids large transients and worsening of the interaction during the update times of the decoupling matrix. The presented experimental results of the decoupling algorithm on the Adv+ prove the effectiveness of the proposed design procedure by showing that the approach keeps the interaction of the decoupled system sufficiently small such that the interaction between the feedback loops can be neglected in the control design. This consequently allows for control designs with more roll-off, reducing the coupling of noise from the CITF DoFs to the sensitivity of the detector.

Data availability statement





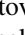
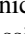


The data cannot be made publicly available upon publication due to legal restrictions preventing unrestricted public distribution. The data that support the findings of this study are available upon reasonable request from the authors.

Acknowledgments

The authors gratefully acknowledge the Italian Istituto Nazionale di Fisica Nucleare (INFN), the French Centre National de la Recherche Scientifique (CNRS) and the Netherlands

Organization for Scientific Research, for the construction and operation of the Virgo detector and the creation and support of the EGO consortium. The authors also gratefully acknowledge research support from these agencies as well as by the Spanish Agencia Estatal de Investigación, the Consellera d'Innovació, Universitats, Ciència i Societat Digital de la Generalitat Valenciana and the CERCA Programme Generalitat de Catalunya, Spain, the National Science Centre of Poland and the Foundation for Polish Science (FNP), the European Commission, the Hungarian Scientific Research Fund (OTKA), the French Lyon Institute of Origins (LIO), the Belgian Fonds de la Recherche Scientifique (FRS-FNRS), Actions de Recherche Concertées (ARC) and Fonds Wetenschappelijk Onderzoek—Vlaanderen (FWO), Belgium.

ORCID iDs

Mathyn van Dael  <https://orcid.org/0000-0002-6061-8131>
 Bas Swinkels  <https://orcid.org/0000-0002-3066-3601>
 Diego Bersanetti  <https://orcid.org/0000-0002-7377-415X>
 Julia Casanueva  <https://orcid.org/0000-0002-2948-5238>
 Maddalena Mantovani  <https://orcid.org/0000-0002-4424-5726>
 Piernicola Spinicelli  <https://orcid.org/0000-0001-8078-6047>
 Camilla de Rossi  <https://orcid.org/0000-0002-5825-472X>
 Tom Oomen  <https://orcid.org/0000-0001-7721-4566>

References

- Aasi J *et al* 2015 Advanced LIGO *Class. Quantum Grav.* **32** 074001
- Acernese F *et al* 2023 Advanced Virgo plus: future perspectives *J. Phys.: Conf. Ser.* **2429** 012040
- Bersanetti D, Boldrini M, Diaz J C, Freise A, Maggiore R, Mantovani M and Valentini M 2022 Simulations for the locking and alignment strategy of the DRMI configuration of the Advanced Virgo Plus detector *Galaxies* **10** 115
- Black E D 2001 An introduction to Pound-Drever-Hall laser frequency stabilization *Am. J. Phys.* **69** 79–87
- Desoer C and Wang Y-T 1980 On the generalized Nyquist stability criterion *IEEE Trans. Autom. Control* **25** 187–96
- Grosdidier P and Morari M 1986 Interaction measures for systems under decentralized control *Automatica* **22** 309–19
- Hung Y S and MacFarlane A G J 1982 *Multivariable Feedback: A Quasi-Classical Approach* (Springer)
- Lee J, Hyun Kim D and Edgar T F 2005 Static decouplers for control of multivariable processes *AIChE J* **51** 2712–20
- MacFarlane A G J 1970 Commutative controller: a new technique for the design of multivariable control systems *Electron. Lett.* **6** 121–3
- Owens D H 1978 *Feedback and Multivariable Systems* (Peter Peregrinus Ltd)
- Packard A and Doyle J 1993 The complex structured singular value *Automatica* **29** 71–109
- Pintelon R and Schoukens J 2012 *System Identification: A Frequency Domain Approach* (Wiley)
- Stoef J, Ertveldt J, Oomen T and Schoukens J 2017 Tensor methods for MIMO decoupling and control design using frequency response functions *Mechatronics* **45** 71–81
- Vaes D, Swevers J and Sas P 2004 Optimal decoupling for MIMO-controller design with robust performance *Proc. 2004 American Control Conf.* vol 5 pp 4601–6
- Valentini M 2023 The longitudinal control for the Advanced Virgo Plus gravitational wave detector *PhD Thesis* Trento U
- van Dael M *et al* 2025 Control of the laser frequency in the Virgo interferometer: dynamic noise budgeting for controller optimization *Astropart. Phys.* **164** 103028

van Dael M, Witvoet G, Swinkels B, Pinto M, Casanueva J, Bersanetti D, Mantovani M, Vardaro M and Oomen T 2022 Design for interaction: factorized Nyquist based control design applied to a gravitational wave detector *Proc. 2022 Modelling, Estimation and Control Conf.*

Zames G 1966 On the input-output stability of time-varying nonlinear feedback systems part one: Conditions derived using concepts of loop gain, conicity and positivity *IEEE Trans. Autom. Control* **11** 228–38